

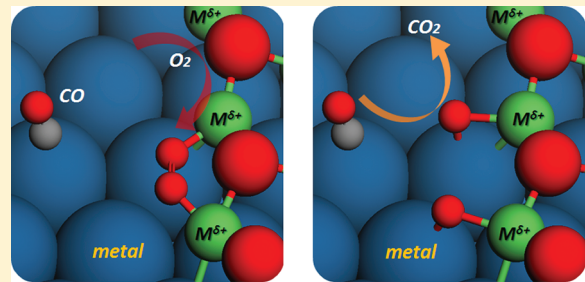
Theoretical Study of the Role of a Metal–Cation Ensemble at the Oxide–Metal Boundary on CO Oxidation

Dapeng Sun,^{†,‡} Xiang-Kui Gu,^{†,‡} Runhai Ouyang,^{†,‡} Hai-Yan Su,^{†,‡} Qiang Fu,[†] Xinhe Bao,[†] and Wei-Xue Li*,^{†,‡}

[†]State Key Laboratory of Catalysis, Dalian Institute of Chemical Physics, Chinese Academy of Sciences, Dalian 116023, China

[‡]Center for Theoretical and Computational Chemistry, Dalian Institute of Chemical Physics, Chinese Academy of Sciences, Dalian 116023, China

ABSTRACT: Identification of the active sites in heterogeneous catalysis is important for a mechanistic understanding of the structure–reactivity relationship and rationale of the design of new catalysts, but remains challenging. Among others, the boundaries at metal nanoparticles and supported oxides were found to be important and attributed to the active sites in various catalytic reactions. To reveal the nature of the active sites at the boundaries, the catalytic role of the inverse 3d transition-metal oxide nanoislands on Pt(111) for low-temperature CO oxidation was studied by density functional theory calculations. A characteristic Pt–cation ensemble at the oxide/metal boundaries as the active sites is identified. In Pt–cation ensembles, coordinate-unsaturated (CUS) cations exposed at the edges of oxide nanoislands are highly active for O₂ adsorption and dissociation, and less-reactive Pt binds modestly with dissociated O responsible for the facile CO oxidation. Inverse VIIIB-oxide/Pt boundaries exhibit high activities for low-temperature CO oxidation, and the corresponding activity decreases gradually from Fe to Co to Ni. The results rationalize a wide range of the experimental findings. To take advantage of the high oxidizing activity of low-valent VIIIB cations, FeO/Pt and CoO/Pt catalysts are appropriate for the reactions under oxygen-poor conditions, whereas NiO/Pt for the reactions under oxygen-rich conditions. The dependence of the activity and valence state of the Pt–cation ensemble at the oxide/metal boundaries is discussed, and the insight of the metal–cation ensemble as the active sites is highlighted.



1. INTRODUCTION

In heterogeneous catalysis, identification of the active sites is important for a mechanistic understanding of the structure–reactivity relationship and rationale of the design of new catalysts.^{1,2} The characteristic of the active sites may change depending on the reactions and catalysts. For instance, defects (or step edges) of supported metal nanoparticles were often attributed to the active sites due to the presence of highly active low coordination sites.^{3–6} The bimetallic alloy catalysts have also been studied widely to separate the active sites and tune the corresponding activity/selectivity.^{7–9} For metal nanoparticles supported on oxides,^{10–13} the nature of the active sites becomes more complex because supports may not only affect the activity and stability but also participate directly into the reaction. For instance, for CO low-temperature oxidation on TiO₂-supported Au nanoparticles,¹⁴ the reaction was suggested to occur at the boundary between the metal nanoparticles and the supports. However, unambiguous identification of the active sites and the role of the supports are not trivial due to the uncertainties of the size and morphology of the metal nanoparticles, in addition to the possible metal–support interaction.¹⁵

To bridge material and pressure gaps, yet taking advantage of surface science apparatus and first-principles density functional

theory (DFT) calculations, oxide grown on metal substrates (so-called inverse oxide/metal model catalysts) has been adopted and studied extensively.^{16–19} In particular, various oxide nanoislands have been fabricated successfully on the metal substrates.^{20–29} Compared to the activity of the bare metal substrates and supported oxides alone, the inverse oxide nanoislands/metal systems were found to be more active. Recently, our experiments found that Pt(111)-supported FeO nanoislands²⁷ exhibited high CO oxidation activity at 273 K; moreover, the conversion was found to be proportional to the specific peripheries of the grown FeO nanoislands. Coordinate-unsaturated (CUS) ferrous species exposed at the edge of the FeO nanoislands were identified as the active sites for activation of the O₂ molecule.^{27,30} Our further experiments found that Pt(111)-supported NiO nanoislands^{31,32} also showed a good activity for CO oxidation at 320 K with even better stability. Despite extensive studies of the inverse oxide nanoislands/metal systems so far, the nature of the active sites, in particular, the role of the CUS cations exposed at the edge of the oxide nanoislands as well as the metal substrates on the activity,

Received: January 28, 2012

Revised: March 13, 2012

Published: March 13, 2012

remains elusive. It is also unclear how valence states and compositions of the oxides as well as its interfacial interaction with substrates affect the activities. Last but not least, the dependence of the stability of the active sites on the reaction conditions also calls for detailed study.

To shed light on these questions, we performed a systematic DFT study for low-temperature CO oxidation on inverse 3d transition-metal (TM) oxide/Pt(111). To see the dependence on compositions, all 3d TMs in the periodic table were considered. On the basis of well-studied FeO/Pt(111)^{27,33–39} and other 3d TM oxides grown on metal substrates,^{31,32,40–43} all 3d TM oxides on Pt(111) were assumed as the bilayer form with a Pt-3d TM-O stacking sequence, and the corresponding valence states for 3d TM cations were lower than 2⁺. For the inverse oxide/metal system considered, a generic metal–cation ensemble at the oxide/metal boundaries is identified to be essential for the site separation and high activity. In this ensemble, the CUS cations exposed at the edge of the oxide islands are highly active for O₂ adsorption and dissociation, while the less-reactive Pt binds modestly with dissociated O responsible for the facile CO oxidation. We found that inverse VIIIB-oxide/Pt boundaries exhibit high activities, and the activity gradually decreases from Fe to Co to Ni. Taking advantage of the high oxidizing activity of low-valent VIIIB cations, FeO/Pt and CoO/Pt catalysts are suitable for the reactions under oxygen-poor conditions, whereas NiO/Pt for the reactions under oxygen-rich conditions. The dependence of the activity and valence states on the 3d transition metal is discussed and highlighted. In the following, a brief introduction of the computational details is given in section 2, and the results are reported in section 3. The discussions are given in section 4, and then conclusions are given finally.

2. COMPUTATIONAL DETAILS

Density functional theory calculations were performed using the Vienna Ab-initio Simulation Package (VASP),^{44,45} employing the all-electron projected augmented wave (PAW) potentials^{46,47} and the Perdew–Wang 91 (PW91)⁴⁸ exchange-correlation functional. Since most of the 3d transition metals (except Cu and Zn) have strong magnetic moment properties, spin polarization is considered for all of them for simplicity. The wave function was expanded by a plane wave with a kinetic cutoff of 400 eV and density cutoff of 800 eV. During iterative diagonalization of the Kohn–Sham Hamiltonian, the Methfessel–Paxton method⁴⁹ of population of the partial occupancies with a width of 0.2 eV was used to improve the convergence, and the total energy is extrapolated to absolute zero temperature correspondingly.

The in-plane Pt lattice constant of 2.818 Å (corresponding 3.985 Å for bulk Pt lattice constant) is employed in the present work. To construct the interface between 3d transition-metal oxide (TMO) and Pt(111), taking into account their lattice mismatch yet remaining affordable in available computational resources, a TMO ribbon with an average in-plane lattice constant of 3.254 Å for all TMO considered is attached to the Pt(111) substrate, forming a (2 $\sqrt{3}$ × 5) rectangular supercell with dimensions of 14.09 Å × 9.76 Å, as indicated in Figure 1. In the TMO ribbon, there are three columns of TM atoms (nine TM atoms overall) contacting with the Pt substrate and two columns of oxygen atoms (six oxygen atoms overall) above. To prevent the unrealistic size effect from the finite width of TMO ribbon, the horizontal *x* and *y* coordinates of 3d TM atoms at the rightmost side of the TMO column and Pt atoms

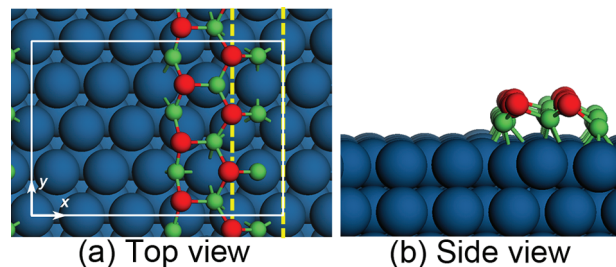


Figure 1. Schematic structure of the inverse TMO/Pt(111) system in top view (a) and side view (b). The supercell used is indicated by a white rectangle with in-plane *x* and *y* axes. The blue, red, and green spheres represent Pt, O, and 3d TMs atoms, respectively.

underneath were frozen. A three-Pt-layer slab was employed to simulate the metal substrate, and the bottom two Pt layers were fixed at their bulk truncated position. All other atoms and the reactants adsorbed on the one side of the slab were fully relaxed until the residual forces were less than 0.03 eV/Å. The overall thickness of the three Pt layers and TMO ribbon was about 8 Å, which was separated by a 12 Å vacuum along the *z* direction. A dipole correction was applied to cancel the artificial interaction from the periodicity. For the Brillouin zone integration, a well-tested special *k*-point (0.25, -0.25, 0) was used. To compare with the bare Pt(111) surface, a five-layer Pt(111)-(2 × 2) slab was studied. The bottom two Pt layers were fixed while residual atoms were optimized until the residual forces were less than 0.02 eV/Å. A (6 × 6 × 1) Γ -centered Monkhorst–Pack grid was used for the Brillouin zone integration.

The activity of the CUS cations exposed at the left edge of the TMO ribbon was studied. The adsorption energy was calculated as

$$E_{\text{ads}} = E_{\text{tot}} - E_{\text{slab}} - E_{\text{mol}}$$

where E_{tot} , E_{slab} , and E_{mol} are calculated total energies of the adsorbate–substrate system, substrate slab, and the adsorbates in gas phase, respectively. The climbing image nudged elastic band (CI-NEB) method^{50,51} was used to calculate the barriers E_b for elementary reactions, such as O₂ dissociation and CO oxidation with dissociated atomic O, and the corresponding reaction energies were given by ΔE_r .

For the interface model, our test calculations showed that an increase of the vacuum to 20 Å led to the variation of the adsorption energy and reaction energy of less than 20 meV in maximum, and negligible for the barrier and the bond length at the transition state. Using the denser *k*-point sampling (3 × 4 × 1), the variation of the adsorption energy, reaction energy, and barrier is less than 30, 50, and 20 meV, respectively, while negligible for the bond length at the transition state again. All these show that the above setup is well-converged. Finally, we note that the correction of the on-site Coulomb repulsion for 3d electrons via DFT+U^{36,37,52} was not considered in the present work, because there are no well-tested *U* values for all 3d TM oxides available. However, a spin-polarized calculation was justified by the small difference with DFT+U calculation for FeO/Pt(111).^{27,30} For adsorption at the FeO/Pt(111) interface, calculated adsorption energies for O₂ and CO are -1.48 and -1.47 eV for the former one, and -1.55 and -1.47 eV for the latter one (*U* = 4 and *J* = 1), respectively. The stronger O₂ binding comparable to CO was found in both cases. For CoO/Pt(111) and NiO/Pt(111), the O₂ binding energy decreases to -1.20 and -0.89 eV for the spin-polarized

calculation, and -1.10 and -0.94 eV for $U = 4$ and $J = 1$ calculation, while the CO adsorption was less affected. The gradual decrease of O_2 competitive adsorption from Fe to Co to Ni were found in both spin-polarized and DFT+U calculations. These benchmarks show that the general trend is well described by the spin-polarized calculation.

3. RESULTS

3.1. CO Adsorption on 3d TMO/Pt(111). We first studied CO adsorption on 3d TMO/Pt(111) interfaces. On the bare Pt surface, only CO adsorption at the top site⁵³ was considered for comparison. Optimized CO is perpendicular to the surface, and the calculated adsorption energy is -1.65 eV. CO adsorption is very weak on the TMO surface, and this indicates that corresponding surface could not act as the efficient adsorption sites. For CO adsorption at the TMO/Pt(111) boundaries, optimized configurations are 3d TM dependent. For Sc and Ti, adsorbed CO prefers the Pt hollow sites but tilts toward the TMO edge, as shown in Figure 2a. The calculated O-TM

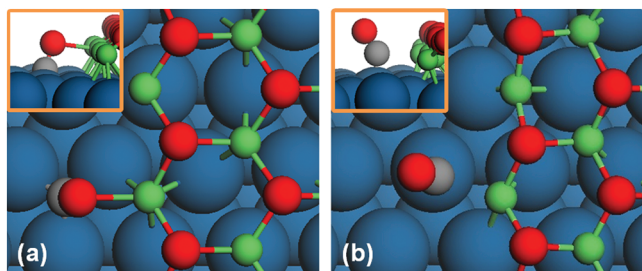


Figure 2. Schematic structures (top view) for CO adsorption at the TMO/Pt(111) boundaries (the insets show the side view). Panel (a) refers to Sc and Ti. Panel (b) refers to V, Cr, Mn, Fe, Co, Ni, Cu, and Zn. The blue, red, green, and dark gray spheres represent Pt, O, 3d TMs, and C atoms, respectively.

bond lengths of the tilted CO are 2.17 and 2.03 Å for Sc and Ti, and the corresponding adsorption energies are -2.48 and -2.09 eV, respectively. The strong binding and tilted configuration toward the CUS cations comes from the high activity of the groups IIIB and IVB elements at low valence states.

For the right side of 3d TMs, such as V, Cr, Mn, Fe, Co, Ni, and Cu, CO adsorption at the boundaries are also tilted, but against the exposed CUS cations (Figure 2b). The C–Pt bond lengths of the tilted CO on Pt top are slightly longer than that of upright CO on bare Pt(111) by about 0.1 Å, which results in a weaker binding by about 0.1 eV than that of bare Pt(111) (Table 1). The backward tilted configuration of CO adsorption originates from a comparably lower activity of the corresponding CUS cations than that of Sc and Ti. The weaker binding and the backward configuration of CO adsorption at the TMO/Pt boundaries alleviate CO poisoning and leave room for adsorption of other reactants, such as O_2 , as discussed below.

Finally, for ZnO/Pt(111), the calculated CO adsorption energy at the boundaries is of no difference compared with that of bare Pt(111). In other words, the presence of ZnO nanoislands has no influence on the bonding strength and configuration of CO adsorption on Pt nearby, which is understandable because of the nobleness of the full filled d-band Zn.

Table 1. Calculated Average Adsorption Energies for CO, O_2 , and Atomic O at the TMO/Pt(111) Boundaries^a

| E_{ads} (eV) | CO | O_2 | O |
|----------------|---------|---------|---------|
| Sc | -2.48 | -5.84 | -2.92 |
| Ti | -2.09 | -6.47 | -3.24 |
| V | -1.58 | -6.12 | -3.06 |
| Cr | -1.56 | -4.57 | -2.29 |
| Mn | -1.34 | -1.46 | -1.42 |
| Fe | -1.47 | -1.48 | -1.37 |
| Co | -1.62 | -1.20 | -1.35 |
| Ni | -1.48 | -0.89 | -1.02 |
| Cu | -1.52 | -0.64 | -0.63 |
| Zn | -1.64 | -0.73 | -0.73 |
| Pt(111) | -1.65 | -0.77 | -0.95 |

^aThe energy reference is CO and O_2 in gas phase. The results on Pt(111) are given at the bottom for comparison.

3.2. O_2 Adsorption and Activation on 3d TMO/Pt(111).

The competitive adsorption and subsequent dissociation of an oxygen molecule are crucial for low-temperature CO oxidation. On bare Pt(111)-(2 × 2), there are several stable sites for O_2 adsorption with similar energies, which could easily transform from one to another with a barrier of less than 0.2 eV. Taking one of the favorable structures, for example, the two O atoms bind to the adjacent Pt atoms with an O–O bond length of 1.37 Å, which is 0.13 Å longer than that in the gas phase. The calculated O_2 adsorption energy is -0.77 eV, much weaker than CO adsorption (-1.65 eV) at the same coverage of 0.25 ML. Though the calculated barrier for O–O bond breaking is only 0.51 eV, the elementary step would be prevented in the presence of CO, for instance, at low temperature because of CO poisoning.

Now we address O_2 adsorption at the TMO/Pt(111) boundaries. We found that the CUS cations exposed at the TMO edge are highly active for molecular oxygen adsorption and dissociation. For the left 3d TMs of Sc, Ti, V, and Cr, the O_2 molecule was found dissociated directly without a barrier and bound to the exposed CUS cations. The elementary reaction was strongly exothermic, and the corresponding dissociative adsorption energies (with respect to O_2 in gas phase) are -5.84 , -6.47 , -6.12 , and -4.57 eV/ O_2 for Sc, Ti, V, and Cr, respectively (Table 1).

For 3d TMs of Mn, Fe, Co, and Ni, the stable molecular adsorption at the TMO/Pt boundaries was found, and calculated adsorption energies (per O_2 molecule) have decreasing values of -1.46 (Mn), -1.48 (Fe), -1.20 (Co), and -0.89 eV (Ni), which are all stronger than that on Pt(111) (-0.77 eV). The optimized configuration is indicated in Figure 3a, where each O atom of O_2 binds to one exposed CUS cation

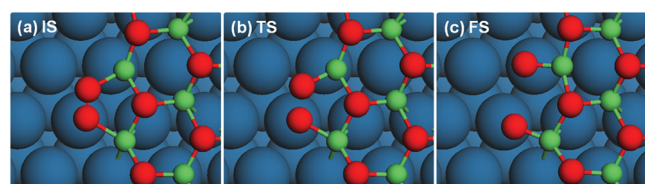


Figure 3. Schematic structures (the top view) of O_2 adsorption at the TMO/Pt(111) boundaries: (a) the initial state, (b) the transition state, and (c) the final state. The blue, red, and green spheres represent Pt, O, and 3d TM atoms, respectively.

and one of them coordinates with the less-reactive Pt atom underneath. Compared to the O–O bond length of 1.37 Å for O₂ on Pt(111), the optimized O–O bond length is slightly longer and varies from 1.39 to 1.44 Å (see Table 2). The longer

Table 2. Reaction Energies ΔE_r and Barriers E_b for O₂ Dissociation at the TMO/Pt(111) Boundaries. The O–O Bond Length of O₂ at the Initial States d (IS) and the Transition States d (TS) are Given^a

| | ΔE_r (eV) | E_b (eV) | d (IS) (Å) | d (TS) (Å) |
|---------|-------------------|------------|--------------|--------------|
| Mn | -1.38 | 0.07 | 1.44 | 1.61 |
| Fe | -1.26 | 0.22 | 1.41 | 1.67 |
| Co | -1.50 | 0.01 | 1.41 | 1.43 |
| Ni | -1.15 | 0.15 | 1.39 | 1.45 |
| Cu | -0.61 | 0.10 | 1.39 | 1.40 |
| Zn | -0.73 | 0.16 | 1.44 | 1.78 |
| Pt(111) | -1.13 | 0.51 | 1.37 | 1.96 |

^aThe results on Pt(111) are given at the bottom for comparison.

bond length and stronger binding of O₂ from the coordination with the CUS cations indicate that molecular adsorption of O₂ is more activated. We found that O₂ dissociation has also been facilitated. Indeed, the calculated dissociation barriers are lower than 0.22 eV, in contrast to 0.51 eV on bare Pt(111). A typical transition state is shown schematically in Figure 3b, where the whole Pt–cation ensemble is involved for O–O bond breaking. This allows the transition states approached without a large stretching of the O–O bond, for instance, 1.43–1.67 Å (Table 2), compared with 1.96 Å on bare Pt(111), a fact that rationalizes the low barriers calculated. The structure of the final state obtained is plotted in Figure 3c, where the dissociated oxygen atoms coordinate with exposed CUS cations and the Pt substrate underneath at the same time. The calculated dissociative adsorption energies with respect to O₂ in the gas phase are -1.42 eV (Mn), -1.37 eV (Fe), -1.35 eV (Co), and -1.02 eV (Ni) per oxygen atom, respectively.

For 3d TMs of Cu and Zn, the corresponding Pt–cation ensemble has little influence on molecular adsorption, as can be seen from calculated energies of -0.64 eV (Cu) and -0.73 eV (Zn). Nevertheless, O₂ dissociation at the Pt–cation ensembles are still facilitated with barriers of less than 0.16 eV (Table 2). The reason is again that the whole Pt–cation ensemble is involved to break the O–O bond.

3.3. CO Oxidation on 3d TMO/Pt(111). We are now addressing the CO oxidation at the TMO/Pt boundaries via the Langmuir–Hinshelwood mechanism. In this mechanism, bare Pt act as the sites for CO adsorption, and the Pt–cation ensembles act as the sites for O₂ activation. First, we analyzed the energetics of the CO oxidation. Taking the reaction energy of CO oxidation in the gas phase (-3.29 eV) as a reference (the horizontal dashed line in Figure 4), if the coadsorption energy of CO and dissociated atomic O at the Pt–cation ensemble is lower than the reaction energy in the gas phase, the subsequent oxidation would be endothermic and cannot take place. From Figure 4, it can be found that the corresponding coadsorption energies at the TMO/Pt(111) boundaries are -5.40, -5.33, -4.64, and -3.84 eV for Sc, Ti, V, and Cr, respectively. All of them are lower than the reaction energy of CO oxidation in the gas phase; namely, CO oxidation cannot occur. This originates from the too strong binding of the dissociated oxygen with the exposed CUS cations, as given in Table 1 and section 3.2. For the remaining TMO/Pt(111)

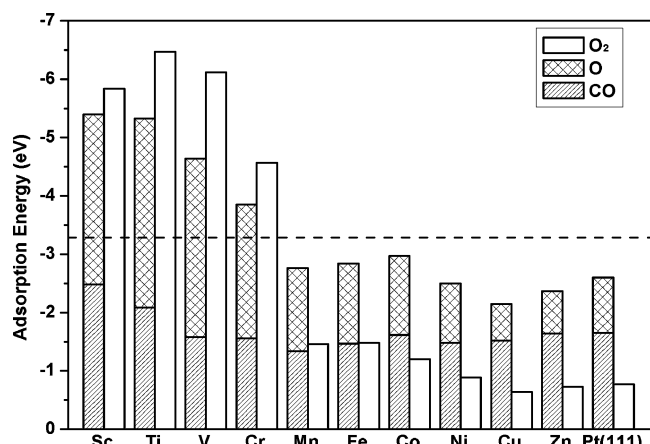


Figure 4. Calculated adsorption energies for CO, O₂, and dissociated O at the TMO/Pt(111) boundaries, and on the Pt(111) surface at last for comparison. The dashed line gives a reference of CO oxidation reaction energy (-3.29 eV) in gas phase. The coadsorption energy of CO and atomic O can be calculated by adding the CO and O columns.

boundaries, including Mn, Fe, Co, Ni, Cu, and Zn, the calculated coadsorption energies are -2.76, -2.84, -2.97, -2.50, -2.15, and -2.37 eV, respectively, which are all higher than the reaction energy of CO oxidation in the gas phase. In other words, the corresponding CO oxidation at these inverse oxide/metal interfaces are energetically likely. The corresponding barriers for CO oxidation are calculated and reported below.

As indicated in Figure 5, there are two types of dissociated oxygen atoms at sites A and B. The initial state (IS) and transition state (TS) at both sites A and B are plotted schematically in Figure 5. The calculated barriers are 0.36, 0.20, 0.41, 0.40, 0.19, and 0.52 eV at site A and 0.90, 0.79, 1.13, 0.98, 0.49, and 0.49 eV at site B for Mn, Fe, Co, Ni, Cu, and Zn, respectively. Independent of the 3d TMs considered (except

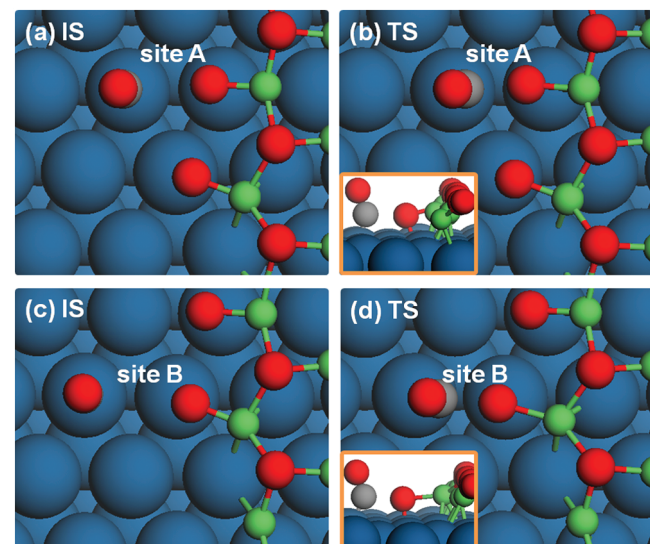


Figure 5. Schematic structures (top view) for CO oxidation with dissociated atomic oxygen at the Pt–cation ensemble at the TMO/Pt(111) boundaries. The left two represent the initial state for reaction with atomic oxygen at sites A (a) and B (c), while the right two (b) and (d) represent the corresponding transition state with the side view shown in the insets.

Zn), all barriers at site A are lower at least by 0.30 eV than those at site B. The bond lengths of formed new O–C bond at the transition state $d(O-C)$ (Table 3) at site A are always

Table 3. Elementary Reaction Energies ΔE_r and Barriers E_b for CO Oxidation with Atomic O at Sites A and B at the TMO/Pt(111) Boundaries^a

| | CO oxidation at site A | | | CO oxidation at site B | | |
|---------|------------------------|---------------|-----------------|------------------------|---------------|-----------------|
| | ΔE_r (eV) | E_b (eV) | $d(O-C)$ (Å) | ΔE_r (eV) | E_b (eV) | $d(O-C)$ (Å) |
| Sc | 1.27 | | | 1.95 | | |
| Ti | 0.71 | | | 1.50 | | |
| V | 0.49 | | | 1.77 | | |
| Cr | 0.04 | | | 0.72 | | |
| Mn | -0.47 | 0.36 | 1.90 | 0.09 | 0.90 | 1.84 |
| Fe | -0.61 | 0.20 | 1.88 | -0.08 | 0.79 | 1.82 |
| Co | -0.47 | 0.41 | 1.83 | -0.13 | 1.13 | 1.81 |
| Ni | -0.74 | 0.40 | 1.86 | -0.44 | 0.98 | 1.83 |
| Cu | -1.37 | 0.19 | 1.99 | -0.50 | 0.49 | 1.92 |
| Zn | -1.27 | 0.52 | 2.10 | -1.02 | 0.49 | 1.99 |
| Pt(111) | -0.57 | 0.85 | 1.99 | | | |

^a $d(O-C)$ is the formed O–C bond length at transition states, and the results on Pt(111) are given at the bottom for comparison.

longer by 0.02–0.11 Å than those of site B. Alternatively, to approach the transition state, less activation is required for CO reaction with oxygen at site A, which is in line with calculated barriers. Consistent with the low barrier at site A, the corresponding reaction energies for CO oxidation are more exothermic. These results tell that, depending on the local registry of the exposed CUS cations with respect to the Pt substrate, the dissociated oxygen at the Pt–cation ensemble may have different reactivities. Nevertheless, all these oxygen species are active for the oxidation reaction.

4. DISCUSSION

For TMO/Pt(111) interfaces studied, the stoichiometric ratio between 3d TMs and oxygen inside the nanoislands is 1:1, and the valence states of 3d TM cations inside of oxide nanoislands are less than 2⁺, taking into account the possible charge transferring with the metal substrate underneath. The elementary reaction steps, including CO adsorption on Pt top, O₂ activation, and oxidation with CO at the TMO/Pt boundaries, are mapped out in detail, presenting a clear bifunctional mechanism. In the following, the dependence of the activity on the composition and valence states of the different inverse oxide/metal systems considered is discussed. To simplify the discussion, the systems are divided into three groups according to the values of their highest valence states. The first group consists of groups IIIB–VIIB (Sc, Ti, V, Cr, and Mn) with the highest valence state of 3⁺ at least. The corresponding bulk oxides are widely used as strong oxidants for various oxidation reactions. The second group consists of group VIIIB (Fe, Co, and Ni) with the highest valence state up to 3⁺. The third group consists of groups IB (Cu) and IIB (Zn), which has the highest valence state of 2⁺. We focus the discussion on the first two groups below since there are well-documented experiments available to compare.

4.1. Groups IIIB–VIIB (Sc, Ti, V, Cr, and Mn). Calculations on these inverse oxide/metal systems show that the CUS cations exposed at the TMO edge with a valence state less than 2⁺ are very active for O₂. Coming O₂ molecules

dissociate spontaneously, except for MnO/Pt(111) with a small barrier of 0.07 eV. The corresponding bonding strengths of dissociated oxygen with the exposed CUS cations are so strong that the subsequent oxidations become endothermic. On the other hand, we note that, for the cations at their highest valence states, they may not be able to activate the O₂ molecule and/or break the O–O bond efficiently. To be more efficient for the oxidation reaction, the optimum valence state should be neither too high to activate O₂ nor too low to oxidize CO. This rationalizes the fact that the defects or, more specifically, the CUS cations in the stable oxide surfaces were often attributed to be the active sites in various reactions. In this context, we note that the interface between oxides and metal catalysts may still play an important role, where the characteristic metal–cation ensemble could be found. Indeed, for low-temperature CO oxidation and water gas shift reaction on TiO₂-supported Au nanoparticles, Ti³⁺ cations together with Au at the interface were found to be highly efficient to activate O₂ and H₂O.^{14,24} On the basis of DFT calculations of CeO₂-supported Au nanoparticles, Ce³⁺ cations and Au at the interface as anchoring sites for O₂ were also proposed to be reactive for CO oxidation.⁵⁴ Similarly, on Rh(111)-supported VO_x nanoislands, the presence of V cations with a valence state higher than 2⁺ at the boundary of the oxide nanoislands was suggested to be active for oxygen activation and subsequent CO oxidation.^{16,23}

4.2. Group VIIIB (Fe, Co, and Ni). For group VIIIB, the valence states in their most stable oxides are 3⁺ for Fe and Co and 2⁺ for Ni, whereas the valence states of the inverse oxide/metal systems studied here are close to 2⁺. The insights obtained in this model study could correlate more directly to the supported nanocatalysts. As shown above, we found that adsorption of CO on Pt in the periphery region is tilted, but against the CUS cations exposed. This not only leaves room for O₂ adsorption and dissociation at the TMO/Pt boundaries but also leads to the adsorption energy of CO (-1.47 to -1.62 eV) to be less sensitive to the element in group VIIIB (Table 1). It is, therefore, the relative activity of the Pt–cation ensembles on O₂ activation that determine the activity of the subsequent CO oxidation. For O₂ adsorption at the Pt–cation ensemble, calculated adsorption energies are -1.48 eV (Fe) and -1.20 eV (Co), competitive with respect to adsorption of CO. Even for Ni, the corresponding adsorption energy (-0.89 eV) remains stronger than adsorption of O₂ on bare Pt(111) (-0.77 eV). As noted above, since the whole Pt–cation ensembles are involved to break the O–O bond, the corresponding barriers for the following O₂ dissociation are small and less than 0.22 eV for all VIIIB elements considered. These indicate that the elementary processes of O₂ adsorption and bond breaking are facile and could compete with CO adsorption at low temperature. Meanwhile, the fact of the dissociated oxygen atom coordinating with the less-reactive Pt atom in the ensemble prevents too strong bonding to be reactive. Indeed, further oxidation with CO adsorbed on the Pt top nearby was found to be exothermic and the corresponding barriers are modest too. All these make the Pt–cation ensemble (Fe, Co, and Ni) be able to oxidize efficiently CO at low temperature. As discussed below, depending on the reaction conditions, the valence states of Fe, Co, and Ni may be subject to further variation, exhibiting the different activities and stabilities.

At the FeO/Pt(111) boundaries, the average dissociative adsorption energy of oxygen is -1.37 eV/O atom. The modest bonding of oxygen by coordinating with less-reactive Pt nearby leads to the following facile CO oxidation with a barrier of 0.20

eV at site A and 0.79 eV at site B, which renders the low-temperature activity. In contrast, for oxygen inside of FeO islands, the calculated dissociative adsorption energy is -3.0 eV/O , which is too strong to be reactive. These results agree well with our previous experimental and theoretical study.²⁷ In that work, the model system with FeO nanoislands grown on Pt(111) was preadsorbed with CO. It was found that the preadsorbed CO on Pt terraces could be removed quickly by O₂ at 273 K. Further experiments found that the conversion was proportional to the specific peripheries of the grown FeO nanoislands, and the FeO nanoislands/Pt(111) boundaries as the active sites were identified unambiguously. As noted before, there is no CO adsorption found on FeO fully covered Pt(111) surfaces.⁵⁵

Formation of FeO nanoislands on Pt(111) comes from their strong interfacial interaction, and the calculated interfacial adhesion energy between FeO and Pt(111) was -1.40 eV per FeO formula.^{27,30} To replace the Pt(111) substrate with highly ordered pyrolytic graphite (HOPG) under the same growth condition (oxygen partial pressure), two-dimensional FeO nanoislands could not be observed. Instead, three-dimensional ferric oxide nanoparticles were found.³³ The reason was attributed to the weak interfacial interaction between iron oxide and HOPG, which could not prevent complete oxidation of iron. Under elevated oxygen partial pressure (higher oxygen chemical potential), the FeO on Pt(111) could be oxidized further and changed from the ferrous to the ferric state, forming, for instance, an O–Fe–O trilayer on Pt(111).^{56,57} The corresponding activity of O–Fe–O fully covered Pt(111) for CO oxidation was lower and took place only at 450 K.⁵⁶ The reaction was proposed to proceed via the Eley–Rideal mechanism where oxygen was replenished by gas-phase O₂ through a Mars–van Krevelen-type mechanism.⁵⁸

To prevent the formation of the less-active ferric species from active ferrous ones, the low oxygen chemical potential is required. This is most likely achieved by, for instance, the selective or partial oxidation reactions, where the oxygen partial pressure would be comparably lower (oxygen-poor condition) than that of complete oxidation under oxygen-rich conditions. Indeed, for CO preferential oxidation in an excess of hydrogen, the complete CO conversion with 100% selectivity at 273 K was found on supported PtFe catalysts, where the presence of ferrous species had been identified under reaction conditions.²⁷ Without the presence of the hydrogen or under higher oxygen partial pressure, the deactivation occurred quickly and no ferrous species were found anymore.⁵⁹

Recently, Zhang and co-workers successfully prepared atomically dispersed Pt on the surface of iron oxide nanocrystallites.¹² It was found that the prepared surface was highly active for CO oxidation in both the presence and the absence of hydrogen at 300 K. Corresponding DFT calculations showed that the origin of the high activity came from the presence of Pt and a defective ferric ensemble on the surface of iron oxide. Defective ferric species were found to be responsible for the activation of oxygen molecules, while the dissociated oxygen atom coordinated simultaneously with defective ferric species and the less-reactive Pt atom, preventing too strong bonding for oxidation of CO coadsorbed on Pt. The importance of the binuclear Pt–Fe cation ensemble for the low-temperature activity can be seen again.

For NiO/Pt(111), the calculated O₂ adsorption energy at the NiO edge decreases to -0.89 eV , higher than that of Pt(111) (-0.77 eV), but much lower than that of FeO/Pt(111) (-1.48 eV).

This indicates that, though competitive adsorption of O₂ with respect to CO is improved on NiO/Pt(111) compared to Pt(111), it is less efficient than FeO/Pt(111). Furthermore, the barrier of CO oxidation with dissociated oxygen at both sites A and B are about 0.2 eV higher than those of FeO/Pt(111). These two factors lead to the overall lower reactivity on NiO/Pt(111). Concerning the interfacial interaction between NiO and Pt(111), which is related to the stability of NiO grown, the calculated interfacial adhesion energy was -0.96 eV per NiO formula, which remains considerable, but smaller than that of FeO/Pt(111). Though this indicates that NiO grown on Pt(111) may be less stable and prone to further oxidation, the fact that the highest valence state of stable nickel oxide 2⁺ makes NiO grown on Pt(111) reluctant to further oxidation. In other words, the NiO on Pt(111) would be rather stable even under elevated oxygen partial pressures and suitable for oxidation reaction under oxygen-rich conditions.

These analyses rationalize well our experimental findings.^{31,32} Indeed, the highly dispersed NiO nanoislands prepared on Pt(111) exhibited a high CO oxidation activity at room temperature. Meanwhile, after the reaction was repeated several times, there was no pronounced change in the reactivity and structure, which indicates good stability of the prepared NiO nanoislands. Under the oxygen-rich condition, complete CO conversion on NiO nanoislands dispersed on Pt surfaces took place at 320 K, which was slightly lower than supported PtFe nanocatalysts where complete CO conversion by oxygen with 100% selectivity occurred already at 273 K in an excess of hydrogen.²⁷

Compared to FeO/Pt(111) and NiO/Pt(111), the calculated O₂ adsorption energy at the CoO/Pt(111) boundaries is weaker than the former one, but remains stronger than the latter one (Table 1). The corresponding activity for the elementary reaction of CO + O oxidation is lower than with FeO/Pt, but similar with NiO/Pt(111) (Table 3). These indicate that the activity of CoO/Pt would be lower than FeO/Pt, but higher than NiO/Pt. Since CoO is prone to be oxidized further to 3⁺ under oxygen-rich conditions, CoO/Pt would be the good catalyst for the oxidation reaction under oxygen-poor conditions, for instance, preferential oxidation in an excess of hydrogen. This was indeed found in previous experiments where the preferential CO oxidation took place at 313⁶⁰ or 380 K,⁶¹ depending on the preparation conditions and supports.

5. CONCLUSIONS

In summary, we performed a systematic first-principles study of the low-temperature CO oxidation on the inverse 3d TM oxide/Pt, and the importance of the oxide and metal boundaries are highlighted. A characteristic metal–cation ensemble at the 3d TMO/Pt boundaries as the active sites is identified. In the metal–cation ensemble, the coordinate-unsaturated cations exposed at the oxide edges are highly active for O₂ activation and free from CO poisoning. On the other hand, the less-reactive Pt atoms in the ensemble coordinate with the dissociated oxygen, a fact that does not make oxygen too strong bind to be active for CO oxidation. We find that the inverse VIIIB-oxide/Pt boundaries exhibit a high activity for low-temperature CO oxidation; moreover, the activity decreases gradually from Fe to Co to Ni. To take advantage of the high oxidizing activity of low-valent VIIIB cations, FeO/Pt and CoO/Pt are appropriate for the reactions under oxygen-poor conditions, whereas NiO/Pt for the reactions under oxygen-rich conditions. Since the activity and stability of the

metal–cation ensemble depend sensitively on their composition, valence state, interfacial interaction between metals and oxides, and the reaction conditions, the insights revealed here are valuable for rationalizing the design of the supported bimetallic catalysts. Further experimental and theoretical work along this direction is promising and worth exploring.

AUTHOR INFORMATION

Corresponding Author

*Tel: (+86)411-8437-9996. Fax: (+86)411-8469-4447. E-mail: wxli@dicp.ac.cn.

Notes

The authors declare no competing financial interest.

ACKNOWLEDGMENTS

The financial support from the National Natural Science Foundation of China (21173210, 20923001, 21103164) is acknowledged.

REFERENCES

- (1) Shetty, S.; van Santen, R. A. *Top. Catal.* **2010**, *53*, 969.
- (2) Thomas, J. M. *J. Chem. Phys.* **2008**, *128*, 182502.
- (3) Honkala, K.; Hellman, A.; Remediakis, I. N.; Logadottir, A.; Carlsson, A.; Dahl, S.; Christensen, C. H.; Norskov, J. K. *Science* **2005**, *307*, 555.
- (4) Hammer, B. *Phys. Rev. Lett.* **1999**, *83*, 3681.
- (5) Lei, Y.; Mehmood, F.; Lee, S.; Greeley, J.; Lee, B.; Seifert, S.; Winans, R. E.; Elam, J. W.; Meyer, R. J.; Redfern, P. C.; Teschner, D.; Schlögl, R.; Pellin, M. J.; Curtiss, L. A.; Vajda, S. *Science* **2010**, *328*, 224.
- (6) Remediakis, I. N.; Lopez, N.; Norskov, J. K. *Angew. Chem., Int. Ed.* **2005**, *44*, 1824.
- (7) Greeley, J.; Mavrikakis, M. *Nat. Mater.* **2004**, *3*, 810.
- (8) Su, H.-Y.; Gu, X.-K.; Ma, X.; Zhao, Y.-H.; Bao, X.-H.; Li, W.-X. *Catal. Today* **2011**, *165*, 89.
- (9) Su, H. Y.; Bao, X. H.; Li, W. X. *J. Chem. Phys.* **2008**, *128*, 194707.
- (10) Fu, Q.; Saltsburg, H.; Flytzani-Stephanopoulos, M. *Science* **2003**, *301*, 935.
- (11) Date, M.; Okumura, M.; Tsubota, S.; Haruta, M. *Angew. Chem., Int. Ed.* **2004**, *43*, 2129.
- (12) Qiao, B.; Wang, A.; Yang, X.; Allard, L. F.; Jiang, Z.; Cui, Y.; Liu, J.; Li, J.; Zhang, T. *Nat. Chem.* **2011**, *3*, 634.
- (13) Haruta, M.; Yamada, N.; Kobayashi, T.; Iijima, S. *J. Catal.* **1989**, *115*, 301.
- (14) Green, I. X.; Tang, W. J.; Neurock, M.; Yates, J. T. *Science* **2011**, *333*, 736.
- (15) Chen, M. S.; Goodman, D. W. *Acc. Chem. Res.* **2006**, *39*, 739.
- (16) Schoiswohl, J.; Surnev, S.; Netzer, F. *Top. Catal.* **2005**, *36*, 91.
- (17) Freund, H. J.; Pacchioni, G. *Chem. Soc. Rev.* **2008**, *37*, 2224.
- (18) Chen, M. S.; Kumar, D.; Yi, C. W.; Goodman, D. W. *Science* **2005**, *310*, 291.
- (19) Street, S. C.; Xu, C.; Goodman, D. W. *Annu. Rev. Phys. Chem.* **1997**, *48*, 43.
- (20) Li, W.-X.; Hammer, B. *Chem. Phys. Lett.* **2005**, *409*, 1.
- (21) Kinnunen, N. M.; Hirvi, J. T.; Suvanto, M.; Pakkanen, T. A. *J. Phys. Chem. C* **2011**, *115*, 19197.
- (22) Sock, M.; Surnev, S.; Ramsey, M. G.; Netzer, F. P. *Top. Catal.* **2000**, *14*, 15.
- (23) Schoiswohl, J.; Eck, S.; Ramsey, M. G.; Andersen, J. N.; Surnev, S.; Netzer, F. P. *Surf. Sci.* **2005**, *580*, 122.
- (24) Rodriguez, J. A.; Ma, S.; Liu, P.; Hrbek, J.; Evans, J.; Perez, M. *Science* **2007**, *318*, 1757.
- (25) Yang, F.; Graciani, J.; Evans, J.; Liu, P.; Hrbek, J.; Sanz, J. F.; Rodriguez, J. A. *J. Am. Chem. Soc.* **2011**, *133*, 3444.
- (26) Jaramillo, T. F.; Jørgensen, K. P.; Bonde, J.; Nielsen, J. H.; Horch, S.; Chorkendorff, I. *Science* **2007**, *317*, 100.
- (27) Fu, Q.; Li, W. X.; Yao, Y. X.; Liu, H. Y.; Su, H. Y.; Ma, D.; Gu, X. K.; Chen, L. M.; Wang, Z.; Zhang, H.; Wang, B.; Bao, X. H. *Science* **2010**, *328*, 1141.
- (28) Surnev, S.; Allegretti, F.; Parteder, G.; Franz, T.; Mittendorfer, F.; Andersen, J. N.; Netzer, F. P. *ChemPhysChem* **2010**, *11*, 2506.
- (29) Xu, L.; Ma, Y.; Zhang, Y.; Jiang, Z.; Huang, W. *J. Am. Chem. Soc.* **2009**, *131*, 16366.
- (30) Gu, X.-K.; Ouyang, R.; Sun, D.; Su, H.-Y.; Li, W.-X. *ChemSusChem* **2011**, DOI: 10.1002/cssc.201100525.
- (31) Mu, R.; Fu, Q.; Xu, H.; Zhang, H.; Huang, Y.; Jiang, Z.; Zhang, S.; Tan, D.; Bao, X. *J. Am. Chem. Soc.* **2011**, *133*, 1978.
- (32) Mu, R.; Guo, X.; Fu, Q.; Bao, X. *J. Phys. Chem. C* **2011**, *115*, 20590.
- (33) Yao, Y.; Fu, Q.; Wang, Z.; Tan, D.; Bao, X. *J. Phys. Chem. C* **2010**, *114*, 17069.
- (34) Knudsen, J.; Merte, L. R.; Grabow, L. C.; Eichhorn, F. M.; Porsgaard, S.; Zeuthen, H.; Vang, R. T.; Laegsgaard, E.; Mavrikakis, M.; Besenbacher, F. *Surf. Sci.* **2010**, *604*, 11.
- (35) Merte, L. R.; Grabow, L. C.; Peng, G.; Knudsen, J.; Zeuthen, H.; Kudernatsch, W.; Porsgaard, S.; Lægsgaard, E.; Mavrikakis, M.; Besenbacher, F. *J. Phys. Chem. C* **2011**, *115*, 2089.
- (36) Giordano, L.; Pacchioni, G.; Goniakowski, J.; Nilius, N.; Rienks, E. D. L.; Freund, H. *J. Phys. Rev. B* **2007**, *76*, 075416.
- (37) Ouyang, R.; Li, W.-X. *Phys. Rev. B* **2011**, *84*, 165403.
- (38) Zhang, W.; Li, Z.; Luo, Y.; Yang, J. *J. Phys. Chem. C* **2009**, *113*, 8302.
- (39) Vurens, G. H.; Maurice, V.; Salmeron, M.; Somorjai, G. A. *Surf. Sci.* **1992**, *268*, 170.
- (40) Agnoli, S.; Sambi, M.; Granozzi, G.; Schoiswohl, J.; Surnev, S.; Netzer, F. P.; Ferrero, M.; Ferrari, A. M.; Pisani, C. *J. Phys. Chem. B* **2005**, *109*, 17197.
- (41) Allegretti, F.; Franchini, C.; Bayer, V.; Leitner, M.; Parteder, G.; Xu, B.; Fleming, A.; Ramsey, M. G.; Podloucky, R.; Surnev, S.; Netzer, F. P. *Phys. Rev. B* **2007**, *75*, 224120.
- (42) Schoiswohl, J.; Zheng, W.; Surnev, S.; Ramsey, M. G.; Granozzi, G.; Agnoli, S.; Netzer, F. P. *Surf. Sci.* **2006**, *600*, 1099.
- (43) Gragnaniello, L.; Barcaro, G.; Sementa, L.; Allegretti, F.; Parteder, G.; Surnev, S.; Steurer, W.; Fortunelli, A.; Netzer, F. P. *J. Phys. Chem. B* **2011**, *134*, 184706.
- (44) Kresse, G.; Hafner, J. *Phys. Rev. B* **1993**, *48*, 13115.
- (45) Kresse, G.; Furthmuller, J. *Phys. Rev. B* **1996**, *54*, 11169.
- (46) Blochl, P. E. *Phys. Rev. B* **1994**, *50*, 17953.
- (47) Kresse, G.; Joubert, D. *Phys. Rev. B* **1999**, *59*, 1758.
- (48) Perdew, J. P.; Chevary, J. A.; Vosko, S. H.; Jackson, K. A.; Pederson, M. R.; Singh, D. J.; Fiolhais, C. *Phys. Rev. B* **1992**, *46*, 6671.
- (49) Methfessel, M.; Paxton, A. T. *Phys. Rev. B* **1989**, *40*, 3616.
- (50) Henkelman, G.; Uberuaga, B. P.; Jonsson, H. *J. Chem. Phys.* **2000**, *113*, 9901.
- (51) Henkelman, G.; Jonsson, H. *J. Chem. Phys.* **2000**, *113*, 9978.
- (52) Dudarev, S. L.; Botton, G. A.; Savrasov, S. Y.; Humphreys, C. J.; Sutton, A. P. *Phys. Rev. B* **1998**, *57*, 1505.
- (53) Feibelman, P. J.; Hammer, B.; Nørskov, J. K.; Wagner, F.; Scheffler, M.; Stumpf, R.; Watwe, R.; Dumesic, J. *J. Phys. Chem. B* **2000**, *105*, 4018.
- (54) Kim, H. Y.; Lee, H. M.; Henkelman, G. *J. Am. Chem. Soc.* **2011**, *134*, 1560.
- (55) Ma, T.; Fu, Q.; Su, H. Y.; Liu, H. Y.; Cui, Y.; Wang, Z.; Mu, R. T.; Li, W. X.; Bao, X. H. *ChemPhysChem* **2009**, *10*, 1013.
- (56) Sun, Y. N.; Qin, Z. H.; Lewandowski, M.; Carrasco, E.; Sterrer, M.; Shaikhutdinov, S.; Freund, H. *J. J. Catal.* **2009**, *266*, 359.
- (57) Giordano, L.; Lewandowski, M.; Groot, I. M. N.; Sun, Y. N.; Goniakowski, J.; Noguera, C.; Shaikhutdinov, S.; Pacchioni, G.; Freund, H. *J. Phys. Chem. C* **2010**, *114*, 21504.
- (58) Sun, Y. N.; Giordano, L.; Goniakowski, J.; Lewandowski, M.; Qin, Z. H.; Noguera, C.; Shaikhutdinov, S.; Pacchioni, G.; Freund, H. *J. Angew. Chem., Int. Ed.* **2010**, *49*, 4418.
- (59) Xu, H.; Fu, Q.; Yao, Y.; Bao, X. *Energy Environ. Sci.* **2012**, DOI: 10.1039/C1EE02393D.

- (60) Wang, C.; Li, B.; Lin, H.; Yuan, Y. *J. Power Sources* **2012**, *202*, 200.
- (61) Ko, E.-Y.; Park, E. D.; Lee, H. C.; Lee, D.; Kim, S. *Angew. Chem., Int. Ed.* **2007**, *46*, 734.